

# Dopant-Free Partial Rear Contacts Enabling 23% Silicon Solar Cells

James Bullock, Yimao Wan, Mark Hettick, Xu Zhaoran, Sieu Pheng Phang, Di Yan, Hanchen Wang, Wenbo Ji, Chris Samundsett, Ziv Hameiri, Daniel Macdonald, Andres Cuevas, and Ali Javey\*

Over the past five years, there has been a significant increase in both the intensity of research and the performance of crystalline silicon devices which utilize metal compounds to form carrier-selective heterocontacts. Such heterocontacts are less fundamentally limited and have the potential for lower costs compared to the current industry dominating heavily doped, directly metalized contacts. A low temperature ( $\leq 230$  °C),  $\text{TiO}_x/\text{LiF}_x/\text{Al}$  electron heterocontact is presented here, which achieves  $\text{m}\Omega\text{cm}^2$  scale contact resistivities  $\rho_c$  on lowly doped n-type substrates. As an extreme demonstration of the potential of this heterocontact, it is trialed in a newly developed, high efficiency n-type solar cell architecture as a partial rear contact (PRC). Despite only contacting  $\approx 1\%$  of the rear surface area, an efficiency of greater than 23% is achieved, setting a new benchmark for n-type solar cells featuring undoped PRCs and confirming the unusually low  $\rho_c$  of the  $\text{TiO}_x/\text{LiF}_x/\text{Al}$  contact. Finally, in contrast to previous versions of the n-type undoped PRC cell, the performance of this cell is maintained after annealing at 350–400 °C, suggesting its compatibility with conventional surface passivation activation and sintering steps.

improving the performance of this technology. For example, materials such as metal oxides, nitrides, and fluorides have been demonstrated to form electron and hole selective interfaces when applied to c-Si.<sup>[1–7]</sup> Such an approach has potential benefits over conventional heavily doped direct-metallization approaches, including lower processing temperatures, simpler contact formation, and the removal of fundamental limitations, such as Auger recombination and free carrier absorption.<sup>[8,9]</sup> In addition, the unique interface properties of some metal compound/c-Si interfaces have even enabled novel solar cell architectures, for example, n-type c-Si cells with undoped partial rear contacts (PRCs).<sup>[10,11]</sup> This specific architecture utilizes a near-ideal surface passivation layer, such as hydrogenated silicon nitride  $\text{SiN}_x$ ,<sup>[12]</sup> to cover the vast majority of the rear surface which

## 1. Introduction

Recent advancements in carrier-selective heterocontacts for crystalline silicon (c-Si) photovoltaics (PV) have highlighted opportunities for utilization of materials-based approaches in

can greatly reduce the average surface recombination factor  $J_0$  and increase the rear reflection. Only a small percentage of the area is contacted, typically  $< 5\%$ , where electrons flow to be collected. An n-type undoped PRC cell structure was not previously attainable due to the tendency of n-type c-Si to form an interface potential barrier under direct metallization, which resulted in prohibitively high contact resistivity  $\rho_c$ . The first successful demonstration of this cell came after a breakthrough in low resistance interfaces to n-type c-Si with a low work function  $\text{LiF}_x/\text{Al}$  electrode. This contact was used to fabricate an undoped PRC cell attaining an efficiency of 20.6% with a PRC covering only  $\approx 1\%$  of the rear surface.<sup>[11]</sup> The next evolutionary step in this cell structure was the integration of a passivation layer at the PRC interface. This came with the introduction of a  $\text{TiO}_x/\text{Ca}/\text{Al}$  contact,<sup>[10]</sup> which was found to provide both reduced surface recombination and low contact resistivity, enabling an efficiency of 21.8%. Following on from these early developments, there exist three major avenues to easily improve the electron PRC: i) reduction in the PRC interface recombination and resistivity; ii) increase in the PRC material's stability to thermal stressors; and iii) increasing the rear surface reflectivity via appropriate choice of PRC materials.

This article introduces the next in this family of carrier selective interfaces, which targets the abovementioned three issues. To address this a  $\text{TiO}_x/\text{LiF}_x/\text{Al}$  heterocontact is developed and integrated into a PRC cell shown in **Figure 1a**. The

Dr. J. Bullock, Dr. Y. Wan, M. Hettick, X. Zhaoran, H. Wang, W. Ji, Prof. A. Javey

Department of Electrical Engineering and Computer Sciences  
University of California  
Berkeley, CA 94720, USA

E-mail: ajavey@berkeley.edu

Dr. J. Bullock, Dr. Y. Wan, M. Hettick, X. Zhaoran, H. Wang, W. Ji, Prof. A. Javey

Materials Sciences Division  
Lawrence Berkeley National Laboratory  
Berkeley, CA 94720, USA

Dr. Y. Wan, Dr. S. P. Phang, Dr. D. Yan, C. Samundsett,  
Prof. D. Macdonald, Prof. A. Cuevas

Research School of Engineering  
The Australian National University (ANU)  
Canberra, Australian Capital Territory 2602, Australia

Dr. Z. Hameiri

University of New South Wales  
Kensington, New South Wales 2052, Australia

 The ORCID identification number(s) for the author(s) of this article can be found under <https://doi.org/10.1002/aenm.201803367>.

DOI: 10.1002/aenm.201803367

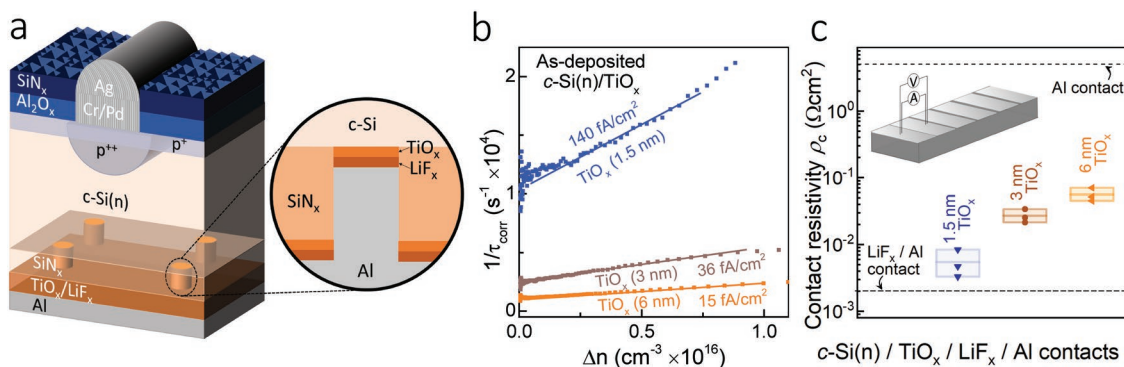


**Figure 1.** a) Conceptual schematic of an n-type PRC cell, the right panel shows a zoom-in of the PRC interface. b) Auger corrected inverse carrier lifetime  $1/\tau_{\text{corr}}$  versus excess carrier density  $\Delta n$  used for  $J_{0c}$  extraction of three  $\text{TiO}_x$  passivated silicon wafers (n-type  $1 \Omega\text{cm}$ ) with different thicknesses of  $\text{TiO}_x$ . The extracted  $J_{0c}$  values are listed beside each dataset. c) Extracted  $\rho_c$  of three different  $\text{TiO}_x/\text{LiF}_x/\text{Al}$  heterocontacts on silicon wafers (n-type  $1 \Omega\text{cm}$ ). Three separate samples are measured for each thickness shown by the solid points. The dotted black lines provide a reference for typical  $\text{LiF}_x/\text{Al}$  and Al contacts and the inset shows a schematic of the TLM structure used in the  $\rho_c$  extraction.

individual materials in this contact provide several potential benefits. Firstly,  $\text{TiO}_x$  layers have been shown to provide excellent surface passivation of c-Si and have exhibited stability in some harsh environments.<sup>[13–16]</sup> It has also been experimentally demonstrated that  $\text{TiO}_x$  interlayers can increase the “S-factor” (reduce the Fermi level pinning) as compared to directly metalized surfaces.<sup>[17]</sup> Secondly, the low work function  $\text{LiF}_x/\text{Al}$  electrode,<sup>[18]</sup> combined with the high permittivity  $\text{TiO}_x$ , can assist in the reduction of barrier heights or even lead to electron accumulation at the c-Si surface. Finally, unlike other low work function electrodes, such as Mg or Ca,  $\text{LiF}_x/\text{Al}$  can provide near-ideal rear-reflection especially when separated from the c-Si absorber with a dielectric spacer (a quantification of this advantage is included in S1 in the Supporting Information). The unique properties of this heterocontact allows the fabrication of a c-Si cell featuring an undoped PRC which achieves a conversion efficiency of above 23% and exhibits thermal stability up to 400 °C.

$\text{TiO}_x$  samples, likely associated with difficulties in exactly replicating nm-scale thicknesses required for the  $\text{TiO}_x$  and  $\text{LiF}_x$  layers. Reference lines for  $\text{LiF}_x/\text{Al}$  and direct Al contacts are included at the bottom and top of the plot, respectively. A clear increase in  $\rho_c$  with the thickness of the  $\text{TiO}_x$  layer is seen, likely a result of the large bulk resistivity of  $\text{TiO}_x$ . Data provided in Figure S2a in the Supporting Information also shows that the addition of the  $\text{LiF}_x$  interlayer is essential in reducing  $\rho_c$  for all thicknesses of  $\text{TiO}_x$ . The results of Figure 1b,c suggest that by controlling the thickness of  $\text{TiO}_x$  a family of heterocontacts may be accessed with  $\rho_c/J_0$  combinations that are suitable for cells with either large-area contacts (low  $J_0$ , moderate  $\rho_c$ ) or small-area contacts (low  $\rho_c$ , moderate  $J_0$ ).

The second avenue to improve on the performance of previous undoped PRC generations is to increase the thermal stability. Figure 2a shows the extracted  $\rho_c$  of a set of  $\text{TiO}_x/\text{LiF}_x/\text{Al}$  heterocontacts as a function of annealing

## 2. Results and Discussion

To initially assess the performance of the  $\text{TiO}_x/\text{LiF}_x/\text{Al}$  heterocontact, a series of contact recombination  $J_0$  and resistivity  $\rho_c$  test structures are fabricated. Figure 1b shows the  $J_0$  values attainable when passivating c-Si with different thicknesses of  $\text{TiO}_x$  (1.5, 3, and 6 nm via atomic layer deposition [ALD] at 230 °C). A clear decrease in  $J_0$  with increasing thickness is seen, as is found for many nm-scale thin films on c-Si. Figure 1c presents extractions of  $\rho_c$  for the same three  $\text{TiO}_x$  thicknesses under a thermally evaporated  $\text{LiF}_x$  ( $\approx 1$  nm)/Al low work-function electrode. For each  $\text{TiO}_x$  thickness, the results from three separate samples are shown, with the box conveying the variation and the middle line providing the average value. Greater relative variation in  $\rho_c$  is seen for thinner

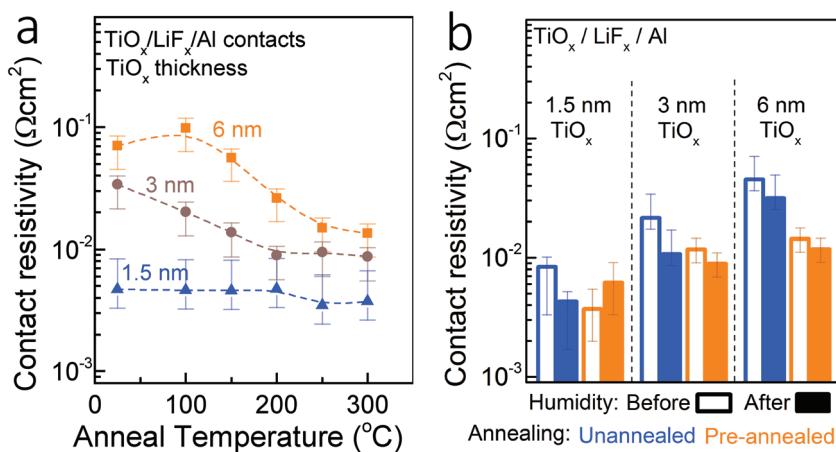


**Figure 2.** a) Evolution of  $\rho_c$  for  $\text{TiO}_x/\text{LiF}_x/\text{Al}$  heterocontacts with three thicknesses of  $\text{TiO}_x$  as a function of hotplate annealing temperature. b)  $\rho_c$  of  $\text{TiO}_x/\text{LiF}_x/\text{Al}$  heterocontacts before (hollow) and after (filled) humidity exposure for three thicknesses of  $\text{TiO}_x$ . The orange and blue bars are representative of samples which did and did not receive a 10 min, 250 °C anneal prior to humidity exposure. Error bars are based on the sample-to-sample variation shown in Figure 1c or the estimated error in the TLM measurement (whichever is largest).

temperature. Interestingly, with increasing anneal temperature, a clear decrease in  $\rho_c$  occurs for heterocontacts with all three thicknesses of  $\text{TiO}_x$ , particularly for thicker  $\text{TiO}_x$  films. This is in contrast to a control sample with 0 nm of  $\text{TiO}_x$ , provided in Figure S2b in the Supporting Information, which shows an increase in  $\rho_c$  at temperatures above 150 °C. This suggests that the  $\text{TiO}_x/\text{LiF}_x/\text{Al}$  contact offers a significant advantage over direct  $\text{LiF}_x/\text{Al}$  contacts in terms of thermal stability; this is particularly relevant for PRC designs where the importance of  $\rho_c$  is increased. Similarly, the  $\text{TiO}_x/\text{LiF}_x/\text{Al}$  heterocontacts are also found to be stable under humidity conditions. Figure 2b shows the measured  $\rho_c$  of  $\text{TiO}_x/\text{LiF}_x/\text{Al}$  heterocontacts taken before and after exposure to 1000 h of 85 °C and 85% relative humidity (RH). The results are provided for all three  $\text{TiO}_x$  thicknesses for samples both with and without a pre-anneal step (250 °C for 10 min). In all cases, no catastrophic changes are measured, with most points falling within the range of error of their unexposed counterparts.

To further explore the role of the  $\text{TiO}_x$  layer, a series of materials-based measurements were performed. Figure 3a shows the valence band (i) and secondary electron cut-off (SEC) (ii) spectra of the as-deposited  $\text{TiO}_x$  layer, measured via X-ray photoelectron spectroscopy (XPS). We note that a  $\text{TiO}_x$  layer of  $\approx 12$  nm was used in these measurements to avoid issues with the XPS sampling depth. A clear band tail is observed in the valence band spectrum, indicative of amorphous/nanocrystalline films (as expected from our previous studies on  $\text{TiO}_x$ ),<sup>[19]</sup> but no sub-bandgap defect band is seen between the valence band and Fermi energy ( $E_v - E_F$  of  $> 3$  eV). The SEC plot shows that the as-deposited  $\text{TiO}_x$  layer has a work function of  $\approx 3.8$  eV, in alignment to that found in previous studies for ex situ films.<sup>[20]</sup> These can be combined with spectroscopic ellipsometry measurements to make an estimation of the band position relative to c-Si. The refractive index of the  $\text{TiO}_x$  film, extracted with a Tauc–Lorentz model,<sup>[21]</sup> is shown in Figure 3b and reveals an optical bandgap of  $\approx 3.35$  eV, similar to that measured for thin  $\text{TiO}_x$  films previously.<sup>[22]</sup>

These results suggest the  $\text{TiO}_x$  layer is n-type and the expected band alignment with c-Si would present a small conduction band offset and a large valence band offset—promoting the selective collection of electrons.

To investigate the measured decrease in  $\rho_c$  with annealing, Figure 3c shows the evolution of the Ti 2p core levels for three  $\text{TiO}_x$  films: i) as-deposited  $\text{TiO}_x$ ; ii)  $\text{TiO}_x/\text{LiF}_x/\text{Al}$  heterocontact after wet chemical removal of the  $\text{LiF}_x/\text{Al}$  layer; and iii) 300 °C annealed  $\text{TiO}_x/\text{LiF}_x/\text{Al}$  heterocontact after wet chemical removal of the  $\text{LiF}_x/\text{Al}$  layer. The as-deposited  $\text{TiO}_x$  film spectrum can be fit well using only the 2p doublet  $\text{Ti}^{4+}$  oxidation state suggesting that it is largely stoichiometric. This stoichiometry is also apparently maintained after depositing, and subsequently removing, the  $\text{LiF}_x/\text{Al}$  layer. However, after annealing with a  $\text{LiF}_x/\text{Al}$  layer on top at 300 °C, a slight reduction in the  $\text{TiO}_x$  film is indicated by the appearance of a small contribution from  $\text{Ti}^{3+}$  oxidation states. The reduction of  $\text{TiO}_x$ , due to interaction with an overlying layer, leading to the formation of oxygen vacancies, has been highlighted as an important factor in other  $\text{TiO}_x$  heterocontacts on c-Si.<sup>[10,23]</sup> A slight shift in the 2p doublet toward lower binding energy is also seen after depositing the  $\text{LiF}_x/\text{Al}$  overlayer and annealing. This could be caused by extrinsic doping due to interface mixing with the  $\text{LiF}_x$  layer. Both reduction of the films and interface mixing may lead to a decreased bulk resistivity of the  $\text{TiO}_x$  layer, which in turn could be responsible for the measured decrease in  $\rho_c$  with annealing.

To test how effectively these contact properties can be transferred to operating devices, the  $\text{TiO}_x/\text{LiF}_x/\text{Al}$  heterocontacts are trialled as a small-area fraction ( $\approx 1\%$ ) PRC in an n-type cell. Figure 4a shows the simulated efficiency (colored contours) of an idealized PRC cell as a function of the  $J_0$  and  $\rho_c$  of the rear contact. The black lines on this plot represent the ideal fraction with which to apply a given  $J_0$  and  $\rho_c$  combination. The superimposed data points, taken from the estimated values in Figure 1, suggest that the thin  $\text{TiO}_x$  layer (1.5 nm) is appropriate for a 1% PRC architecture. As highlighted above,

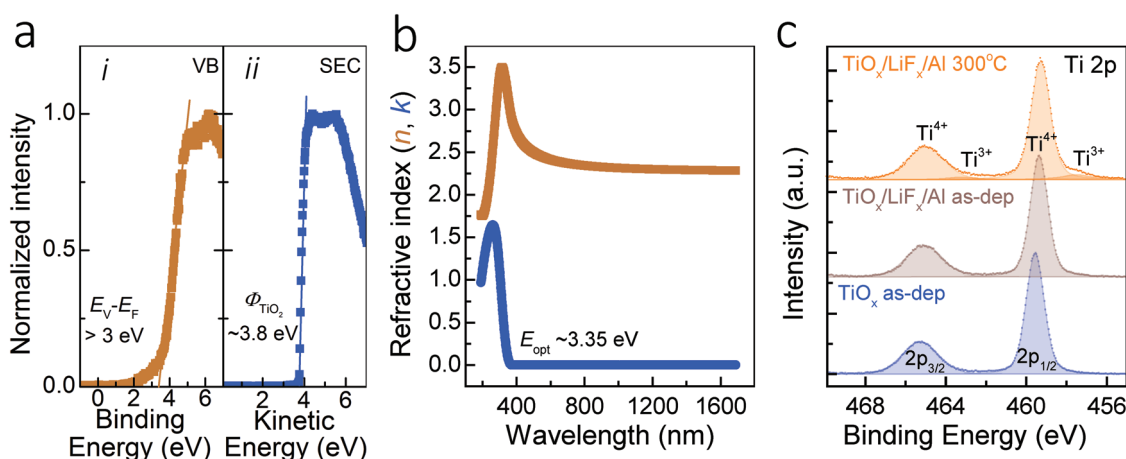


**Figure 3.** a) Measured valence band (i) and secondary electron cut-off (ii) spectrum of the as-deposited  $\text{TiO}_x$  film. b) Tauc–Lorentz modeled refractive index of the as-deposited  $\text{TiO}_x$  film showing an optical bandgap of  $\approx 3.35$  eV. c) Measured Ti 2p core level spectrum of  $\text{TiO}_x$  films after deposition (bottom), capping with a  $\text{LiF}_x/\text{Al}$  (middle) and subsequent annealing at 300 °C (top). The  $\text{LiF}_x/\text{Al}$  layers were removed via a wet chemical etch prior to measurement for the middle and top samples. The shaded region represents the modeled contribution from different oxidation states to the measured spectrum.

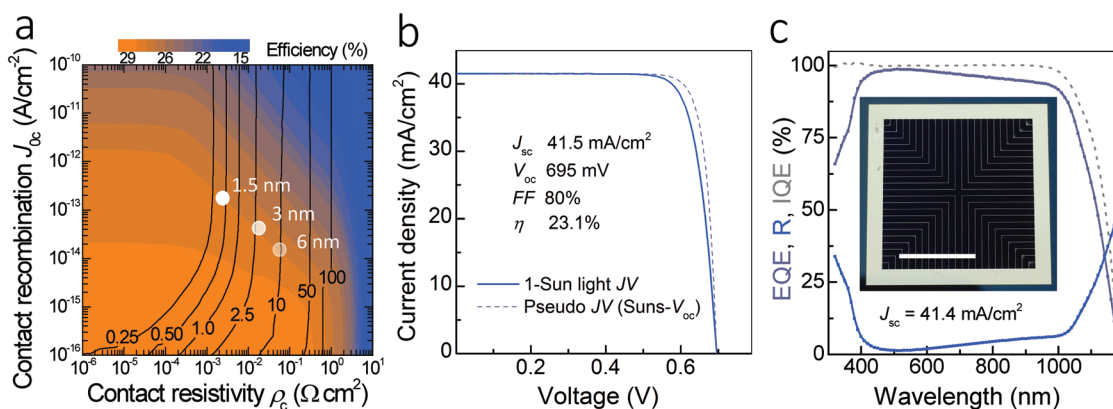


**Figure 4.** a) Simulated ideal efficiency (colored contours) for a silicon solar cell as a function of the rear contact  $\rho_c$  and  $J_{0c}$ . For each combination, an ideal contact fraction is also simulated (black lines). The white data points are representative of potential  $\text{TiO}_x/\text{LiF}_x/\text{Al}$  heterocontacts, with different  $\text{TiO}_x$  thicknesses indicated, using information in Figure 1. b) Measured light JV characteristics of n-type PRC cell collected under standard 1-Sun conditions (solid line) compared the pseudo-JV curve for the same cell measured by Suns- $V_{oc}$  (dashed line). c) Quantum efficiency (QE) analysis showing the wavelength-dependent EQE, IQE, and reflection. The inset provides a photograph of the cell front design and the integrated short circuit current is also listed. The white scale bar represents 1 cm.

an additional possibility not explored here is to use the thicker  $\text{TiO}_x$  layers as larger-area (or even full-area) rear contacts. The thin  $\text{TiO}_x$  PRC is tested by integrating it into a  $2 \times 2 \text{ cm}^2$ , n-type cell with an optimized front-side (the cross-sectional structure of which is depicted in Figure 1a). Figure 4b shows the current density–voltage ( $J$ – $V$ ) plot of the champion cell, measured under standard 1-Sun conditions ( $100 \text{ mW cm}^{-2}$ ,  $25 \text{ }^\circ\text{C}$ , AM 1.5G spectrum). This cell achieves a conversion efficiency of 23.1%—the highest value for this cell class to date. The obtained open circuit voltage  $V_{oc}$  of 695 mV suggest that some level of surface recombination suppression has been maintained at the heterocontact after the anneal. This value is also confirmed by Suns- $V_{oc}$  measurements, shown in the form of a pseudo-JV curve, as a dotted line in Figure 4b. The comparison between the real and pseudo-JV curves of Figure 4b, which indicates the magnitude of series resistance  $R_s$  in the cell, suggests that efficiencies of closer to 24% could be achieved by reducing  $R_s$ . Regardless, the measured fill factor (FF) of 80% is high given the infancy of the structure and confirms that a low  $\rho_c$  has been attained at the PRC. Perhaps the most impressive parameter is the short circuit current density  $J_{sc}$ , reaching  $41.5 \text{ mA cm}^{-2}$ , which falls just below the maximum expected for this cell design. This high  $J_{sc}$  would not be possible without excellent rear reflection, a clear indication of the performance of the  $\text{TiO}_x/\text{LiF}_x/\text{Al}$  rear reflector when combined with the  $\text{SiN}_x$  dielectric spacer. It is important to note that in comparison to previous n-type cells with undoped PRCs, the above presented cell also benefits from significant optimization of other cell regions. For example, the near-ideal front-side metallization design, shown in the inset of Figure 4c, minimizes both optical and electrical losses (more details on the cell preparation can be found in Experimental Section). Figure 4c provides an accompanying quantum efficiency analysis showing the external quantum efficiency (EQE), reflection (R), and internal quantum efficiency (IQE). A comparison  $J_{sc}$  is obtained from the integrated EQE and AM 1.5G product, with a value of  $41.4 \text{ mA cm}^{-2}$  in excellent agreement with the value obtained

via light JV. After accounting for reflection, an IQE of  $\approx 100\%$  is maintained from 300 nm to just before the band edge at 1100 nm—a clear indication of near-ideal carrier collection. The dopant diffused counterpart of this cell is an n-type Passivated Emitter Rear Locally diffused (nPERL) cell which features heavily phosphorus-doped localized contacts at the rear. In comparison to this structure, the  $\text{TiO}_x/\text{LiF}_x/\text{Al}$  nPRC removes the necessity of the high-temperature phosphorus diffusion as well as PRC masking and alignment steps, a significant advantage for this structure.

A crucial component in the success of these cells was post-fabrication annealing. As shown in Figure 5a, a significant improvement in FF is seen after annealing cells for 10 min in forming gas (5%  $\text{H}_2$ ; 95%  $\text{N}_2$ ) within a quartz furnace with a set temperature of  $350 \text{ }^\circ\text{C}$ —a condition chosen to mimic the thermal stress of  $300 \text{ }^\circ\text{C}$  hotplate exposure. Utilizing a forming gas anneal at the end of cell fabrication has become a standard step for diffused junction c-Si solar cells (see, for example, ref. [24]) with benefits including surface passivation activation and contact sintering. Annealing beyond 10 min at  $350 \text{ }^\circ\text{C}$  lead to only minimal additional change. The FF improvement is likely resultant from simultaneous reductions in the front- and rear-side contact resistance. This is in line with the known benefits of sintering electroplated silver contacts (which are used in the front-side metallization). To further investigate the thermal stability of the  $\text{TiO}_x/\text{LiF}_x/\text{Al}$  heterocontact, a representative undoped PRC cell was subjected to additional anneal testing at  $350 \text{ }^\circ\text{C}$  for 180 min. As shown in Figure 5b, no significant change in cell performance was seen over this period and even after an additional 10 min anneal at a  $400 \text{ }^\circ\text{C}$  set temperature. At higher temperatures ( $450 \text{ }^\circ\text{C}$  and above) the performance of the cell degrades rapidly, behavior which is likely resultant from performance degradation in multiple cell regions (i.e., not just the rear  $\text{TiO}_x/\text{LiF}_x/\text{Al}$  PRC). Regardless, the stability exhibited in the  $350$ – $400 \text{ }^\circ\text{C}$  range suggests the compatibility of this heterocontact structure with conventional forming gas anneal steps utilized for surface passivation and contact sintering.

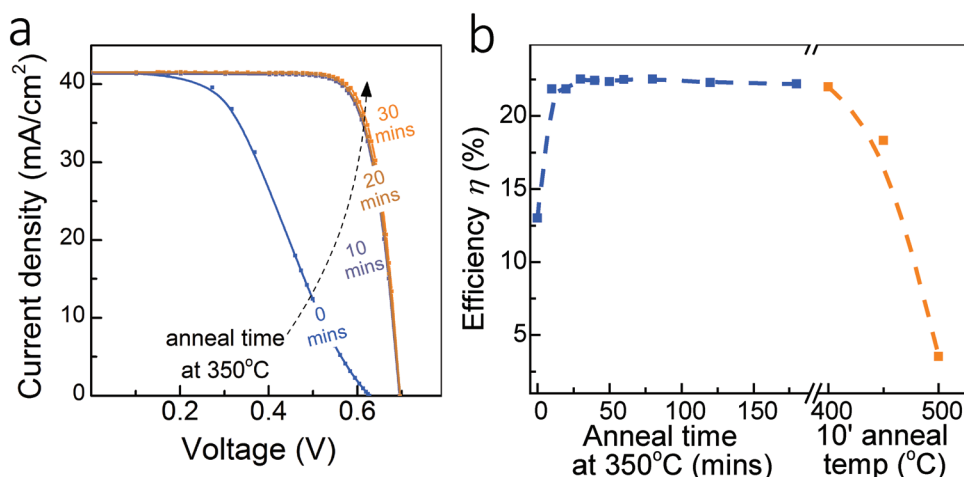


**Figure 5.** a) Evolution in light *JV* behavior as a function of post deposition annealing at 350 °C in a quartz furnace for the n-type PRC cell. b) Change in efficiency of the n-type PRC cell as a function of anneal time and temperature.

### 3. Conclusion

In this study, we have introduced the next iteration in a fast-improving family of electron heterocontacts for c-Si solar cells based on a TiO<sub>x</sub>/LiF<sub>x</sub>/Al layer stack. This heterocontact exhibits low contact resistivity, the possibility of surface passivation, and excellent thermal and humidity stability. To test its effectiveness, it is integrated into a newly developed n-type cell architecture, as an undoped PRC covering just ≈1% of the rear surface area. This optimized 2 × 2 cm<sup>2</sup> cell has been demonstrated with an efficiency of above 23%—a new record for this architecture and for cells employing TiO<sub>x</sub>-based electron contacts in general. Further, this cell maintains its performance after annealing at temperatures up to 400 °C, suggesting its compatibility with standard passivation and sintering anneal steps. These results set a new target for efficiency and thermal stability of the n-type undoped PRC cell and highlight its potential as a high efficiency cell concept.

### 4. Experimental Section

**Contact and Cell Fabrication and Characterization:** Lifetime samples, utilized for the *J*<sub>0</sub> extraction, were fabricated on 1 Ωcm n-type, (100), float zone, c-Si wafers. After standard Radio Corporation of America (RCA) cleaning procedures, samples were dipped in a dilute (≈5%) hydrofluoric acid solution, rinsed, and deposited symmetrically with TiO<sub>x</sub> layers of different thicknesses. The TiO<sub>x</sub> layer was deposited via ALD (Beneq TFS 200) at a temperature of 230 °C, using alternating cycles of titanium tetraisopropoxide (TTIP) and water. A growth rate of ≈0.3 Å per cycle was obtained for this process with 50, 100, and 200 cycles corresponding to the 1.5, 3, and 6 nm films. The effective lifetime of samples was measured after deposition using photoconductance decay (Sinton WCT 120) and the *J*<sub>0</sub> was extracted using the Kane and Swanson method.<sup>[25]</sup> It should be noted that the extracted *J*<sub>0</sub> value may change after the deposition of the LiF<sub>x</sub>/Al layer and subsequent annealing, they are included here as an estimate.

Contact resistivity samples were fabricated in an identical manner to lifetime samples, except that TiO<sub>x</sub> was only deposited on one surface of the 1 Ωcm n-type wafer. Following this, a LiF<sub>x</sub> (≈1 nm)/Al (≈200 nm) stack was deposited via thermal evaporation through a shadow mask to define a transfer-length-method (TLM) pattern. Each TLM strip was isolated via mechanical cleaving on either side to reduce lateral

spreading. Measurements of resistance versus pad spacing were made with a Keithley 2400 source-meter. It should be noted that the accuracy of the TLM approach is compromised when applied to lowly doped wafers, as was the case here. The parallel resistance through the TiO<sub>x</sub> layer was assumed to be negligible. Annealing was performed using sequential 10 min anneals at temperatures between 100 and 300 °C by placing samples directly on a hotplate in air. Humidity exposure for 1000 h at 85 °C 85% RH was performed in an Espec LHU environmental chamber.

The 2 × 2 cm<sup>2</sup> n-type undoped PRC cells were fabricated with a double boron diffusion on the front to create localized heavily doped p<sup>++</sup> regions under the front metal contacts. These front contacts, which only took up ≈1% of the front surface, were defined by photolithography followed by thermal evaporation of a Cr/Pd/Ag stack and lift-off. The stack was thickened via Ag electroplating to reduce the front-side series resistance. An AlO<sub>x</sub>/SiN<sub>x</sub> passivation and antireflection stack was deposited on the front via ALD and plasma-enhanced chemical vapor deposition (PECVD, Oxford PlasmaLab 100), respectively. A rear-side PECVD SiN<sub>x</sub> passivation/dielectric spacer was patterned with small 30 μm diameter holes to the c-Si surface covering less than 1% of the rear surface area. Through these holes, the TiO<sub>x</sub> (1.5 nm)/LiF<sub>x</sub>/Al stack directly contacted the n-type c-Si surface forming the PRC. Following fabrication, the whole cell structure was annealed in a quartz furnace at a set temperature of 350 °C for 30 min in forming gas (5% H<sub>2</sub>, 95% N<sub>2</sub>). This anneal step was chosen to mimic the conditions of a 300 °C hotplate anneal and was found to result in the highest FF without impacting the *V*<sub>oc</sub>. Thermal stressing tests were performed in the same furnace at higher set temperatures.

The 1-Sun *JV* analysis was performed using a Sinton FCT450 under standard conditions (100 mW cm<sup>-2</sup>, 25 °C, AM 1.5G spectrum), the inner edge of the contact periphery, shown in Figure 4c's inset, was used to define the cell area. Suns-*V*<sub>oc</sub> measurements of the cells were taken on a Sinton Suns-*V*<sub>oc</sub> tester. The EQE was measured in a PV Measurements system (model QF/IPCE) with a small sampling area that included a representative percentage of metal finger coverage. Reflection measurements were taken over a large part of the cell area using a Perkin Elmer 1050 spectrophotometer UV-vis spectrophotometer. Solar cell simulations were performed with Quokka2.0,<sup>[26]</sup> utilizing idealized values for all cell regions except the rear contact.

**Materials Characterization:** Three XPS samples were fabricated on highly doped, single-side polished, n-type c-Si wafers. A 12 nm thick TiO<sub>x</sub> layer was deposited on the polished side of all three samples using the same method as above. Following this, two of the three samples were coated with an additional LiF<sub>x</sub> (≈1 nm)/Al stack, one of which was then annealed at 300 °C for 10 min on a hotplate in air. Al and LiF<sub>x</sub> layers were etched prior to XPS measurements using a dilute hydrochloric acid solution at room temperature, following which they were rinsed thoroughly in deionized water.

XPS characterization was performed using a Kratos AXIS spectrometer with hemispherical analyzer and monochromatic Al source. Charge correction was performed using a C 1s reference, and peak positions were fit via Voigt lineshapes and referenced to the NIST XPS database.<sup>[27]</sup> An accelerating bias of 9.0 V was used for the secondary electron cut-off measurement.

Spectroscopic ellipsometry measurements were performed on a J.A. Woollam M-2000 ellipsometer. A Tauc–Lorentz model was used to extract the optical bandgap and refractive index.

## Supporting Information

Supporting Information is available from the Wiley Online Library or from the author.

## Acknowledgements

Materials characterization was supported by the Electronic Materials Programs, funded by the Director, Office of Science, Office of Basic Energy Sciences, Material Sciences and Engineering Division of the US Department of Energy under Contract No. DE-AC02-05CH11231. XPS characterization was performed at the Joint Center for Artificial Photosynthesis, supported through the Office of Science of the US Department of Energy under Award Number DE-SC0004993. Work at the Molecular Foundry was supported by the Office of Science, Office of Basic Energy Sciences, of the US Department of Energy (Contract No. DE-AC02-05CH11231).

## Conflict of Interest

The authors declare no conflict of interest.

## Keywords

selective contacts, silicon photovoltaics, titanium oxide

Received: October 31, 2018

Revised: December 28, 2018

Published online:

- [1] M. Bivour, J. Temmler, H. Steinkemper, M. Hermle, *Solar Energy Mater. Solar Cells* **2015**, *142*, 34.
- [2] J. Bullock, A. Cuevas, T. Allen, C. Battaglia, *Appl. Phys. Lett.* **2014**, *105*, 232109.
- [3] K. A. Nagamatsu, S. Avasthi, G. Sahasrabudhe, G. Man, J. Jhaveri, A. H. Berg, J. Schwartz, A. Kahn, S. Wagner, J. C. Sturm, *Appl. Phys. Lett.* **2015**, *106*, 123906.
- [4] X. Yang, E. Aydin, H. Xu, J. Kang, M. Hedhili, W. Liu, Y. Wan, J. Peng, C. Samundsett, A. Cuevas, S. D. Wolf, *Adv. Energy Mater.* **2018**, *8*, 1800608.
- [5] Y. Wan, C. Samundsett, J. Bullock, T. Allen, M. Hettick, D. Yan, P. Zheng, X. Zhang, J. Cui, J. McKeon, A. Javey, A. Cuevas, *ACS Appl. Mater. Interfaces* **2016**, *8*, 14671.
- [6] C. Battaglia, X. Yin, M. Zheng, I. D. Sharp, T. Chen, S. McDonnell, A. Azcatl, C. Carraro, B. Ma, R. Maboudian, R. M. Wallace, A. Javey, *Nano Lett.* **2014**, *14*, 967.
- [7] J. Bullock, Y. Wan, Z. Xu, S. Essig, M. Hettick, H. Wang, W. Ji, M. Boccard, A. Cuevas, C. Ballif, A. Javey, *ACS Energy Lett.* **2018**, *3*, 508.
- [8] S. C. Baker-Finch, K. R. McIntosh, D. Yan, K. C. Fong, T. C. Kho, *J. Appl. Phys.* **2014**, *116*, 063106.
- [9] A. Richter, S. W. Glunz, F. Werner, J. Schmidt, A. Cuevas, *Phys. Rev. B* **2012**, *86*, 165202.
- [10] T. G. Allen, J. Bullock, Q. Jeangros, C. Samundsett, Y. Wan, J. Cui, A. Hessler-Wyser, S. De Wolf, A. Javey, A. Cuevas, *Adv. Energy Mater.* **2017**, *7*, 1602606.
- [11] J. Bullock, P. Zheng, Q. Jeangros, M. Tosun, M. Hettick, C. M. Sutter-Fella, Y. Wan, T. Allen, D. Yan, D. Macdonald, S. De Wolf, A. Hessler-Wyser, A. Cuevas, A. Javey, *Adv. Energy Mater.* **2016**, *6*, 1600241.
- [12] Y. Wan, K. R. McIntosh, A. F. Thomson, A. Cuevas, *IEEE J. Photovoltaics* **2013**, *3*, 554.
- [13] A. F. Thomson, K. R. McIntosh, *Prog. Photovoltaics* **2012**, *20*, 343.
- [14] B. Liao, B. Hoex, A. G. Aberle, D. Chi, C. S. Bhatia, *Appl. Phys. Lett.* **2014**, *104*, 253903.
- [15] D. Bae, B. Seger, P. C. K. Vesborg, O. Hansen, I. Chorkendorff, *Chem. Soc. Rev.* **2017**, *46*, 1933.
- [16] P. Alén, M. Vehkamäki, M. Ritala, M. Leskelä, *J. Electrochem. Soc.* **2006**, *153*, G304.
- [17] A. Agrawal, J. Lin, M. Barth, R. White, B. Zheng, S. Chopra, S. Gupta, K. Wang, J. Gelatos, S. E. Mohny, S. Datta, *Appl. Phys. Lett.* **2014**, *104*, 112101.
- [18] J. Bullock, M. Hettick, J. Geissbühler, A. J. Ong, T. Allen, C. M. Sutter-Fella, T. Chen, H. Ota, E. W. Schaler, S. De Wolf, C. Ballif, A. Cuevas, A. Javey, *Nat. Energy* **2016**, *1*, 15031.
- [19] X. Yin, C. Battaglia, Y. Lin, K. Chen, M. Hettick, M. Zheng, C.-Y. Chen, D. Kiriya, A. Javey, *ACS Photonics* **2014**, *1*, 1245.
- [20] S. Kashiwaya, J. Morasch, V. Streibel, T. Toupance, W. Jaegermann, A. Klein, S. Kashiwaya, J. Morasch, V. Streibel, T. Toupance, W. Jaegermann, A. Klein, *Surfaces* **2018**, *1*, 73.
- [21] G. E. Jellison Jr., *Thin Solid Films* **1998**, *313–314*, 33.
- [22] Y.-J. Shi, R.-J. Zhang, H. Zheng, D.-H. Li, W. Wei, X. Chen, Y. Sun, Y.-F. Wei, H.-L. Lu, N. Dai, L.-Y. Chen, *Nanoscale Res. Lett.* **2017**, *12*, 243.
- [23] X. Yang, Q. Bi, H. Ali, K. Davis, W. V. Schoenfeld, K. Weber, *Adv. Mater.* **2016**, *28*, 5891.
- [24] J. Zhao, A. Wang, P. Altermatt, M. A. Green, *Appl. Phys. Lett.* **1995**, *66*, 3636.
- [25] D. E. Kane, R. M. Swanson, presented at *Proc 18th IEEE Photovolt. Spec. Conf.*, Las Vegas, USA, October **1985**, pp. 578–583.
- [26] A. Fell, K. C. Fong, K. R. McIntosh, E. Franklin, A. W. Blakers, *IEEE J. Photovoltaics* **2014**, *4*, 1040.
- [27] “NIST X-ray Photoelectron Spectroscopy Database, *NIST Standard Reference Database Number 20*, National Institute of Standards and Technology, Gaithersburg MD, 20899,” can be found under [https://srdata.nist.gov/xps/main\\_search\\_menu.aspx](https://srdata.nist.gov/xps/main_search_menu.aspx), **2000**.